High-Accuracy Inertia and Damping Estimation Method and Testing Equipment for Grid-Forming Converters

Yufan Wang, *Student Member, IEEE*, and Jingyang Fang, *Senior Member, IEEE*

***Abstract*—Grid-forming converters (GFMCs) receive increasing adoption in modern power systems due to their salient advantages, such as grid formulation and improved stability in weak grids. In GFMCs, inertia and damping play an essential role on the frequency regulation of modern grids. As such, the accurate estimation of these parameters is of great value for ensuring system stability, advancing ancillary service markets, and supporting grid-forming standardization. However, existing estimation methods rarely target at GFMCs' inertia and damping, rely on large amounts of data, and lack validations through experiments. In view of this, this article proposes a simple and effective model-based testing method that exploits the inherent relationship between frequency and power. By decoupling inertial power and damping power, the estimation accuracy is greatly improved. Building on this method, we further developed the first grid-forming testing equipment. As verified by experiments, inertia and damping coefficients estimation errors are within 5% and 2% , respectively.**

***Index Terms*—Damping, grid-forming converters (GFMCs), inertia, testing equipment.**

I. Introduction

As RENEWABLE generation continues its upward trend, the generation mix in modern power systems is changing, with synchronous generators (SGs) progressively being replaced by grid-tied power converters. However, grid-tied power converters, e.g., for wind and solar photovoltaics generation, inherently possess zero inertia or damping [1]. Consequently, the inertia and damping of modern power systems, previously contributed by SGs, continue to decline. Nevertheless, inertia and damping play a vital role in modern systems, as they mitigate the rate of change of frequency (RoCoF) and help reduce frequency deviations [2]. The ever-decreasing inertia and damping problem can potentially lead to cascading failures in power systems and even large-scale blackouts. To address the anticipated challenge, ancillary services, such as virtual inertia and virtual damping, become increasingly important in modern power systems [3].

Grid-tied converters are mainly categorized into two types—grid-following and grid-forming converters (GFMCs). Compared with grid-following converters, GFMCs offer salient advantages, such as smooth transition between islanded and grid-tied operation, flexible frequency and voltage control, and improved stability in weak grids [4]. As a result, GFMCs remain on a strong growth trajectory in the foreseeable future and are expected to contribute ancillary services, where inertia and damping serve as two key parameters for performance evaluation. While these parameters have nominal values, practical implementations vary significantly among manufacturers. Differences in control algorithms, hardware limitations, or proprietary logics may deviate actual dynamics. In consequence, the estimation of inertia and damping coefficients of GFMCs is of great value for the following reasons. First, the analysis of system and converter stability necessitates the knowledge of inertia and damping [5]. Second, the accurate estimation of inertia and damping is crucial for ancillary service markets [6]. Third, evolving standards on GFMCs put stringent requirements on inertia and damping tests [7]. Therefore, we expect the accurate estimation of the inertia and damping coefficients of GFMCs.

However, existing inertia estimation methods primarily target at bulky power systems. These methods can broadly be classified into two types—disturbance-based methods and disturbance-free methods. Normally, disturbance-based methods estimate inertia by analyzing the frequency variations caused by frequency events. Two typical disturbance-based are documented in [8] and [9], where the authors estimated inertia derived from the measured RoCoF. However, it should be emphasized that the accurate estimation of RoCoF itself remains as a challenge [8]. To address this shortcoming, an online algorithm based on dynamic regression and hybrid processes was developed to estimate the total inertia after a generator tripping [9]. In addition to generation tripping, some researchers estimated inertia by use of the disturbances caused by three-phase-to-ground faults [10], [11]. Even though the above-mentioned methods demonstrate their capability for inertia estimation, they rely on severe grid faults, which occur infrequently, thus making their implementation and validation challenging [8], [9], [10], [11]. As alternatives, the methods that actively inject disturbance signals have been proposed. For example, Hosaka et al. [12] proposed a

Received 12 August 2025; revised 25 October 2025 and 2 December 2025; accepted 7 January 2026. Date of publication 13 January 2026; date of current version 20 March 2026. This work was supported in part by the National Natural Science Foundation of China under Grant 52377192, Grant 20221017-9, and Grant 12411530110, in part by the Department of Science and Technology of Shandong Province under Grant ZR202210270088, and in part by the Zhejiang Electric Power Research Institute under Grant B311DS25Z007. Recommended for publication by Associate Editor Q. Wei. *(Corresponding author: Jingyang Fang.)*

The authors are with the School of Control Science and Engineering, Shandong University, Jinan 250100, China (e-mail: kzwyf@sdu.edu.cn; jingyangfang@sdu.edu.cn).

Color versions of one or more figures in this article are available at https://doi.org/10.1109/TPEL.2026.3653741.

Digital Object Identifier 10.1109/TPEL.2026.3653741

TABLE I
COMPARISONS OF INERTIA AND DAMPING ESTIMATION METHODS

Methods	Application	Providing Damping Estimation	Physical Experiment	Methods	Application	Providing Damping Estimation	Physical Experiment
[8], [9], [10]	Power systems	×	×	[27]	GFMC	×	×
[11]	Power systems	√	×	[28]	GFMC	×	×
[12], [13], [14], [15], [16], [17], [18]	Power systems	×	×	[29]	GFMC	×	×
[19]	Power systems	√	×	[30]	GFMC	×	×
[20]	Synchronous generator	×	×	[31]	GFMC	×	×
[21]	Synchronous generator	×	Inertia: 10%	[32]	GFMC	√	×
[22]	Synchronous generator	×	Inertia: 5%	Proposed Method	GFMC	√	Inertia: 5% Damping: 2%
[26]	GFMC	×	×				

method that estimates the system inertia by actively injecting active power. Zhang and Xu [13] estimated inertia through a similar approach. Through the disconnection of high-voltage dc interconnectors during normal operation, it is possible to create power disturbances, thereby allowing the estimation of system inertia [14]. However, these methods inevitably disrupt the normal running of power systems, thus being undesirable in practice [12], [13], [14].

In comparison, the disturbance-free methods using environmental measurements have been proposed, which can estimate inertia without incurring extra burdens [15], [16], [17], [18], [19]. For example, the methods proposed in [15], [16], [17] estimate inertia through data. Specifically, Poudyal et al. [15] employed a neural network to estimate regional and system inertia in steady state. In [16], the introduced federated learning method is a machine learning technique where multiple decentralized devices were trained using local data. Schmitt and Lee [17] used the least squares estimation method to extract the inertia coefficient from the system state matrix. A primary limitation of these methods lies in their reliance on a large quantity of data to learn the relationship between inertia and frequency [15], [16], [17]. In addition, Gorbunov et al. [18] developed a model-based disturbance-free method to estimate the inertia coefficient, which necessitates an accurate model of power systems, thus posing challenges under variable operating conditions and parameters. Similarly, as a model-based approach, the method given in [19] largely depends on the order of the model and is very sensitive to operating conditions. Moreover, this method requires a large data measurement window. Importantly, all the aforementioned methods are applicable to power systems rather than converters.

Recently, the methods tailored to the estimation of the inertia of SGs and/or GFMCs have been proposed. The authors in [20], [21], and [22] provided methods exclusively designed for measuring the inertia of SGs. However, the inertia estimation methods for SGs are not directly applicable to GFMCs, as GFMCs exhibit a strong coupling between inertia and damping, unlike the negligible or weakly coupled damping typically assumed for SGs [23], [24]. Furthermore, the absence of rotor-based kinetic energy in GFMCs, combined with their significantly lower overcurrent capability, necessitates the development of dedicated testing methods [25]. The methods in [26] and [27] were developed for estimating the inertia of GFMCs. However, they neglect the impact of damping on inertia. Liu et al. [28] presented a model-based dynamic estimation method for capturing the time-varying inertia of GFMCs. However, it suffers from the inherent delays and estimation errors that reduce measurement precision. Meanwhile, the purely data-driven methods in [29], [30], [31], and [32] attempted to circumvent the damping problem but required substantial amounts of high-quality training data, which are normally unavailable in practice. It is essential to highlight that all the testing methods applicable to GFMCs are only validated via simulations rather than experiments, as summarized in Table I.

This article proposes an inertia and damping estimation method for GFMCs that exploits the inherent relationship between frequency and power. The major contributions of this article are listed as follows.

1) Propose a high-accuracy inertia and damping coefficients testing method based on inertial and damping power decoupling.
2) Design a robust measurement and data processing framework to ensure the accurate estimation of inertia and damping coefficients in the presence of disturbances.

The rest of this article is organized as follows. Section II describes the overall structure of the testing system, which includes the GFMC under test and the testing equipment developed via the proposed method. In Section III, the control implementations of the GFMC under test are detailed, with a particular focus on the analysis of the power coupling mechanism and decoupling method. Section IV introduces the implementation of the testing equipment, with the proposed testing method as

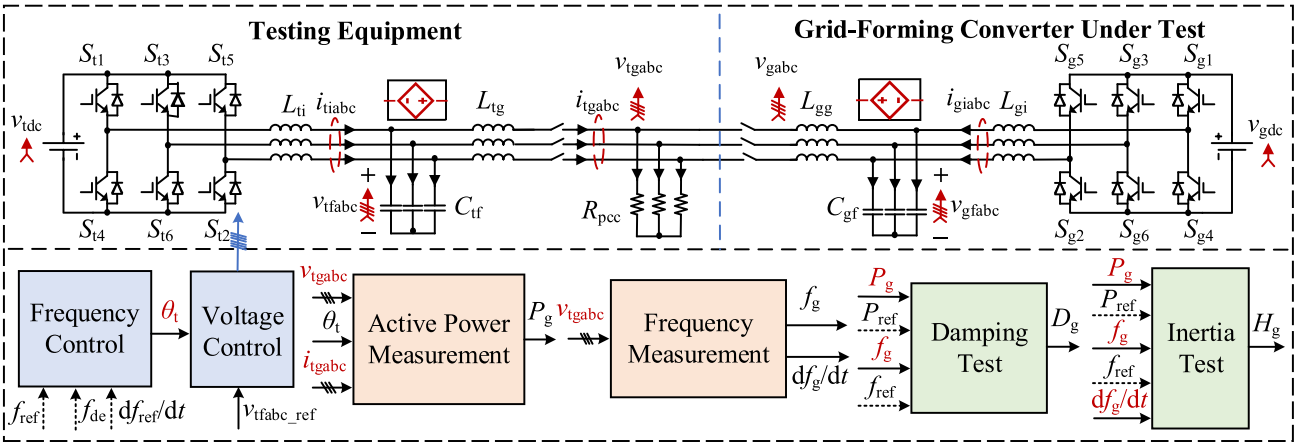

Fig. 1. Overall structure of the testing system.

its core. Section V verifies the effectiveness of the proposed estimation method and testing equipment through simulation and experimental results. Section VI introduces the experimental data processing. Finally, Section VII concludes this article.

II. Overall Structure of the Testing System

The proposed testing system is shown in Fig. 1, which consists of two major components—the developed testing equipment and the GFMC under test, with their connection point linked to a three-phase load R_{pcc}.

A. Main Circuit of the GFMC Under Test

As shown in Fig. 1, the GFMC under test includes six active switches (S_{g1}–S_{g6}) connected to the testing equipment via an *LCL* filter, composed of L_{gi}, C_{gf}, and L_{gg}. The dc bus voltage is denoted as v_{gdc}, while v_{gfabc} and i_{giabc} represent the capacitor voltages and converter-side currents, respectively. Understandably, this converter can provide inertia and damping through control blocks, as detailed in Section III.

B. Main Circuit and Testing Blocks of the Testing Equipment

The main circuit of the proposed testing equipment in Fig. 1 mirrors that of the GFMC under test. The former also includes six active switches (S_{t1}–S_{t6}) and filtering components L_{ti}, C_{tf}, and L_{tg}, which form an *LCL* filter. The dc bus voltage is denoted as v_{tdc}. v_{tfabc} and i_{tiabc} represent the capacitor voltages and converter-side currents, respectively. v_{tgabc} and i_{tgabc} stand for the voltages at and currents injected to the point of common coupling, respectively. Notably, at high-power levels, converter topologies typically differ from those introduced above. In such cases, modular multilevel converters and cascaded h-bridge (CHB) converters are potential candidates, as discussed in [33]. However, most control blocks of the testing equipment remain generally applicable, as described below.

In parallel with the main circuit, the control blocks of the testing equipment can also be visualized in Fig. 1, including the frequency control, voltage control, active power measurement, frequency measurement, damping test, and inertia test blocks. These blocks work in sequence.

First, the frequency and voltage control blocks generate voltages and establish a local grid according to predefined algorithms. Second, the active power and frequency measurement blocks yield the respective power and frequency signals. Third, the damping test block estimates the damping coefficient. Finally, the inertia test block estimates the inertia coefficient.

Specifically, we first design the reference values of the RoCoF $\mathrm{d}f_{\mathrm{ref}}/\mathrm{d}t$, frequency change f_{de}, and reference frequency f_{ref} for the frequency control block, which generates the reference phase angle signal θ_{t}. Upon receiving θ_{t} and the reference voltage $v_{\mathrm{tfabc\_ref}}$, the voltage control block generates PWM control signals. Consequently, the active power measurement block computes the active power P_{g} of the GFMC under test using v_{tgabc}, i_{tgabc}, and θ_{t}. Meanwhile, the frequency measurement block estimates the frequency f_{g} and RoCoF $\mathrm{d}f_{\mathrm{g}}/\mathrm{d}t$ of the GFMC under test through a phase-locked loop. Next, the damping test block exploits P_{g}, f_{g}, f_{ref}, and the reference active power P_{ref} to estimate the damping coefficient D_{g}. Taking leverage of the above inputs, along with $\mathrm{d}f_{\mathrm{g}}/\mathrm{d}t$, the inertia test block finally estimates the inertia coefficient H_{g}. More details on the method and its implementation in the testing equipment will be presented in Section IV.

III. Control Implementations of the GFMC Under Test

This section aims to detail the control scheme of the GFMC under test, including an analysis of the power decoupling mechanism.

The control of the GFMC under test normally includes the inner-loop voltage control and outer-loop power control blocks [1]. The voltage control block tightly tracks the amplitude and phase angle of capacitor voltages v_{gfabc}. The voltage control block is identical to that of the testing equipment, as will be detailed in Section IV. Generally, the outer power control block enables the active power and reactive power to track their references. Notably, most grid-forming power control strategies

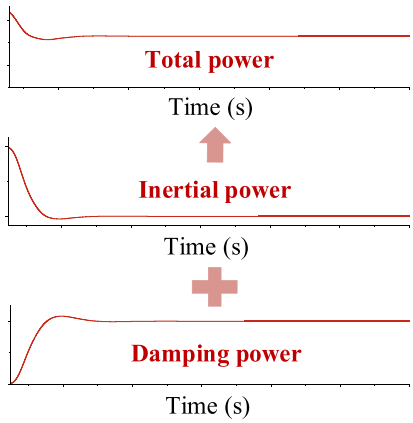

Fig. 2. Power response of the GFMC during transients.

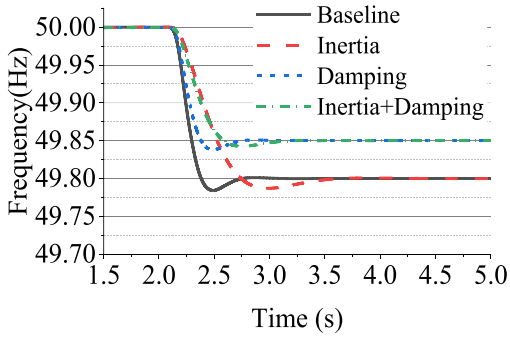

Fig. 3. Effects of inertia and damping on frequency regulation.

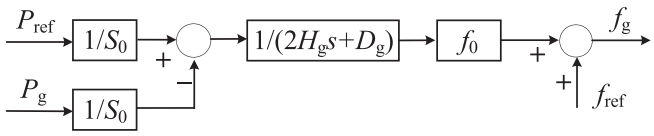

Fig. 4. Active power control of the GFMC under test.

that incorporate inertia and damping share a similar power–frequency relationship. In this section, the virtual synchronous machine (VSM) control is selected as a representative example, since its inertia and damping coefficients are inherently coupled—making the measurement problem more challenging and illustrative.

It is well known that the dynamics of SGs are governed by the classical swing equation as follows [34]:

$$2H_{\mathrm{g}}\frac{\mathrm{d}f_{\mathrm{g\_pu}}}{\mathrm{d}t}=P_{\mathrm{ref\_pu}}-P_{\mathrm{g\_pu}}-D_{\mathrm{g}}\left(f_{\mathrm{g\_pu}}-f_{\mathrm{ref\_pu}}\right) \tag{1}$$

where the subscript pu denotes the per-unit value. H_{g} and D_{g} represent the inertia and damping coefficients, respectively. Alternatively, we can reorganize (1) by their real values as follows:

$$\frac{P_{\mathrm{ref}}-P_{\mathrm{g}}}{S_0}=\frac{2H_{\mathrm{g}}}{f_0}\cdot\frac{\mathrm{d}f_{\mathrm{g}}}{\mathrm{d}t}+D_{\mathrm{g}}\cdot\frac{f_{\mathrm{g}}-f_{\mathrm{ref}}}{f_0} \tag{2}$$

where S_0 and f_0 denote the nominal power and frequency, respectively.

According to (2), the total power change of the GFMC during frequency transients comprises two components—the damping power and inertial power. Specifically, the damping power is proportional to the frequency change, while the inertial power is proportional to the RoCoF, namely,

$$\begin{cases}P_{\mathrm{D}}=\frac{S_0D_{\mathrm{g}}}{f_0}\times\left(f_{\mathrm{g}}-f_{\mathrm{ref}}\right)\\ P_{\mathrm{H}}=\frac{2H_{\mathrm{g}}S_0}{f_0}\times\frac{\mathrm{d}f_{\mathrm{g}}}{\mathrm{d}t}\end{cases} \tag{3}$$

where P_{D} and P_{H} represent the damping power and inertial power, respectively. Fig. 2 visualizes the relationships between the total power and the inertial/damping power components, where the coupling of inertial and damping power is clear.

The effects of inertia and damping on frequency regulation is illustrated in Fig. 3. It can be observed that inertia improves RoCoF, yet without affecting the quasisteady-state frequency. In comparison, damping can reduce frequency deviations during transients and in quasi-steady state without affecting the RoCoF.

Through the active power control of the VSM, the GFMC under test can effectively emulate the inertia and damping characteristics of SGs by duplicating (2) [35], [36], [37], [38]. Consequently, the VSM power control can be reformulated in the complex domain as follows [39]:

$$\frac{P_{\mathrm{ref}}-P_{\mathrm{g}}}{S_0}=\left(2H_{\mathrm{g}}s+D_{\mathrm{g}}\right)\frac{f_{\mathrm{g}}-f_{\mathrm{ref}}}{f_0} \tag{4}$$

where s designates the complex domain notation. With (4), the control block diagram of the tested GFMC is shown in Fig. 4.

IV. Control Implementations of the Testing Equipment

The previous section disclosed the coupling mechanism of inertial power and damping power. This section aims to detail the control scheme of the proposed testing equipment, with a particular focus on the testing method based on power decoupling, which serves as its core.

The control block diagrams of the testing equipment are detailed in Fig. 5. As seen, the frequency control block uses a step signal f_{de} as one of its inputs, which aims to generate a frequency change for damping measurement. On top of that, the frequency control block includes a square wave signal $\mathrm{d}f_{\mathrm{ref}}/\mathrm{d}t$, which yields a frequency f_{t} with a bipolar triangle waveform for inertia measurement. The voltage control block employs PI controllers, where the subscripts d and q represent the d- and q-axis components, respectively. The active power measurement block computes P_{g} using the power calculation equation illustrated in Fig. 5. The essence of the frequency measurement block is a phase-locked loop, which aims to estimate f_{g} and $\mathrm{d}f_{\mathrm{g}}/\mathrm{d}t$, where θ_{g} denotes the measured phase angle.

For damping estimation, the testing equipment generates three-phase voltage signals with a frequency change f_{de}, which varies on the basis of 50 Hz. Subsequently, the testing equipment obtains active power and frequency signals. Based on the analysis of inertial and damping power in Section III, it is evident that the power change is entirely due to damping in quasi-steady state. Therefore, the damping coefficient of the GFMC under

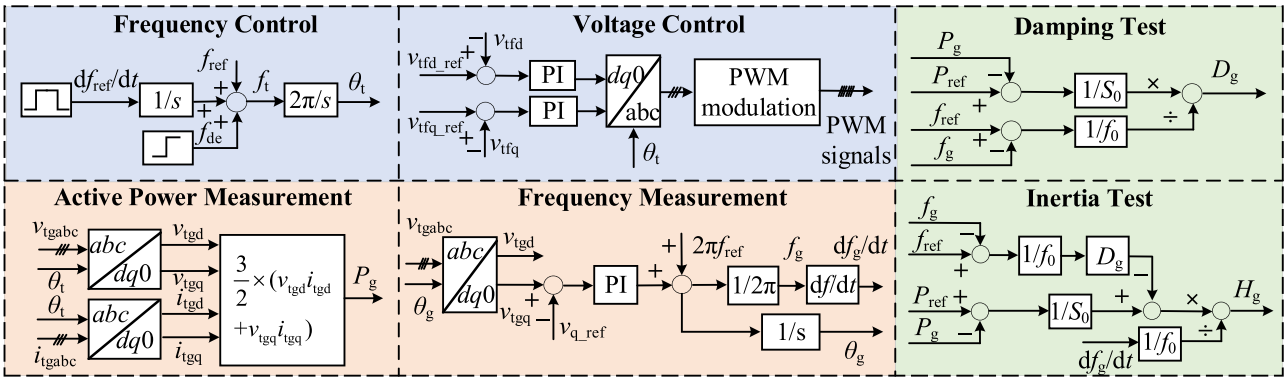

Fig. 5. Control block diagrams of the testing equipment.

test can be determined by the damping testing block. Its core formulation is derived from the damping power calculated from (3). Specifically, P_{D} is defined as the difference between P_{ref} and P_{g}. Thus, the damping coefficient can be calculated via

$$D_{\mathrm{g}} = \frac{(P_{\mathrm{ref}} - P_{\mathrm{g}}) \times \frac{1}{S_0}}{(f_{\mathrm{g}} - f_{\mathrm{ref}}) \times \frac{1}{f_0}}. \tag{5}$$

In experiments, P_{g} is obtained by measuring the voltage and current at the converter output and calculating their product through the active power measurement block, and f_{g} is extracted using a phase-locked loop, which tracks the voltage phase angle and provides the real-time estimation of the frequency. Generally, manufacturers provide the rated frequency and nominal active power of each GFMC.

It is important to note that the denominator in (5) should not be zero, which requires that $f_{\mathrm{g}} \neq f_{\mathrm{ref}}$. With our proposed testing method, this condition is inherently satisfied, because a predefined frequency change is actively injected during the test, ensuring that f_{g} and f_{ref} are not equal.

For the estimation of the inertia coefficient, the testing equipment generates three-phase voltages with a bipolar triangle frequency waveform varying within ± 0.1 Hz around 50 Hz. Afterward, the testing equipment obtains active power, frequency, and RoCoF signals. In this case, the active power change is collectively determined by both damping and inertia. Since the damping coefficient has previously been estimated, we subtract the damping power from the total power change and calculate the inertia coefficient through

$$2H_{\mathrm{g}} = \frac{(P_{\mathrm{ref}} - P_{\mathrm{g}}) \times \frac{1}{S_0} - D_{\mathrm{g}} \times (f_{\mathrm{g}} - f_{\mathrm{ref}}) \times \frac{1}{f_0}}{\frac{df_{\mathrm{g}}}{dt} \times \frac{1}{f_0}}. \tag{6}$$

The above equation is closely related to (3) and (5). In (6), the numerator corresponds to the inertial power, which can be obtained by subtracting the damping power in (5) from the total power change. The denominator refers to the RoCoF signal. The relationships among the numerator, denominator, and inertia coefficient agree with (3).

It should be noted that (6) requires that $\mathrm{d}f_{\mathrm{g}}/\mathrm{d}t$ should not be zero. With our proposed testing method, this condition is inherently satisfied, as a predefined nonzero RoCoF signal is actively injected into the system during the test.

Notably, the proposed method injects a disturbance for accurate estimation. However, this is not a practical concern during the preconnection testing of GFMCs, as such perturbations can easily be introduced without causing adverse effects. Moreover, the method is scalable to system-level applications. By utilizing the real-time measurement of power and frequency, equivalent inertia and damping coefficients can be estimated through online or offline computations. In such scenarios, frequency events, such as grid faults or load changes, can replace deliberate disturbance injection. In addition, an advantage of the proposed disturbance-based approach is that, even in the presence of disturbances, the underlying power–frequency relationship can well be controlled and hence remains unchanged, thus ensuring satisfactory estimation results. This disturbance resilience stems from the structural robustness inherent in the mechanism of the proposed method.

V. Simulation and Experimental Verifications

A. Simulation Results

We developed a MATLAB/Simulink (R2023a) model based on the system schematic and control structure shown in Fig. 1, with system and control parameters detailed in Table II.

In practice, the inertia and damping of GFMCs may vary due to controller tuning, firmware updates, or equipment aging. Therefore, to ensure a reliable validation of the proposed method, we first tested the GFMC with VSM control and three different damping scenarios, where damping coefficients are $D_{\mathrm{g}} = 80$, 100, and 120, respectively. In simulations, it should be emphasized that frequency step signals were injected immediately after the system reached stable parallel operation. Once the system settled down, the proposed method provided accurate and stable estimation. Fig. 6 presents the steady-state simulation results. As illustrated in Fig. 6(a), (b), and (c), the proposed method allows high-accuracy damping estimation with $<1\%$ estimation errors.

After that, we tested three cases with different inertia, where the inertia coefficients are $H_{\mathrm{g}} = 5$ s, 8 s, and 10 s, respectively. The relevant results are shown in Fig. 6(d), (e), and (f), which

TABLE II
PARAMETERS USED IN SIMULATION AND EXPERIMENTAL TESTS

Category	Descriptions	Symbols	Values
Testing equipment	Voltage amplitude	v_{tf}	110 Vrms
Converter under test	Voltage amplitude	v_{gf}	110 Vrms
Testing equipment	DC-link voltage	v_{tdc}	330 V
Converter under test	DC-link voltage	v_{gdc}	330 V
Testing equipment	Filter inductance	L_t	10 mH
Converter under test	Filter inductance	L_g	4 mH
Testing equipment	Filter capacitance	C_t	5 μF
Converter under test	Filter capacitance	C_g	5 μF
Point of Common Coupling	Three-phase load resistance	R_{pcc}	100 Ω

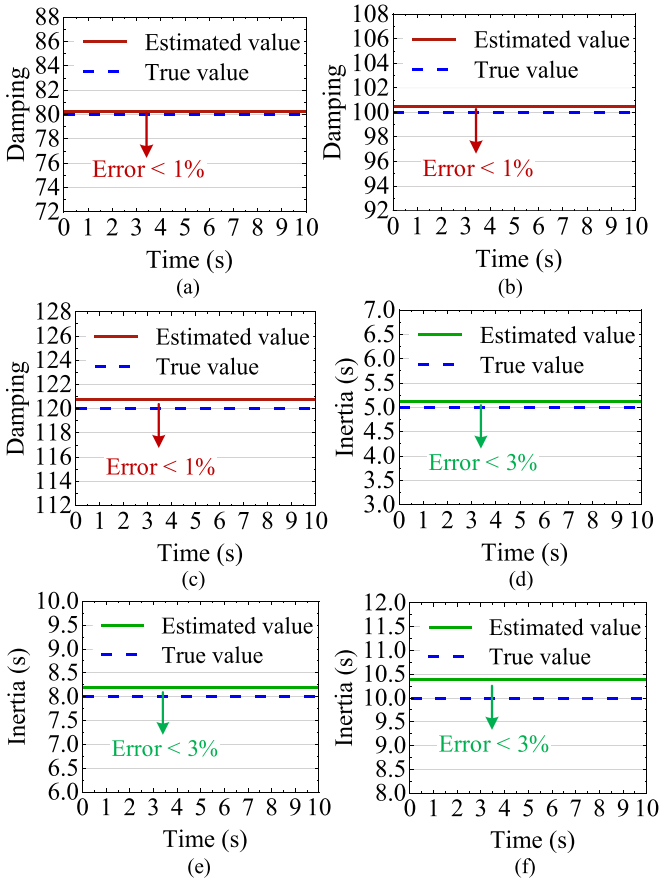

Fig. 6. Simulation results of damping estimation with D_g = (a) 80, (b) 100, and (c) 120, and inertia estimation with H_g = (d) 5 s, (e) 8 s, and (f) 10 s.

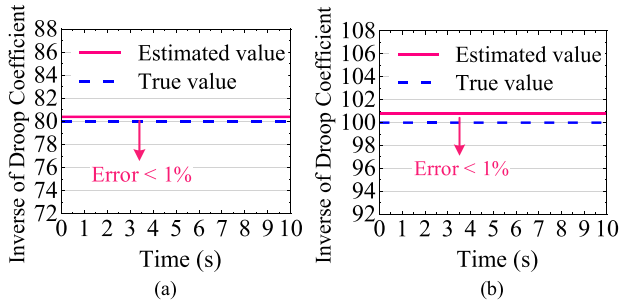

Fig. 7. Simulation results of the equivalent damping estimation with droop control, including the droop coefficients R_g of (a) 0.0125 and (b) 0.01.

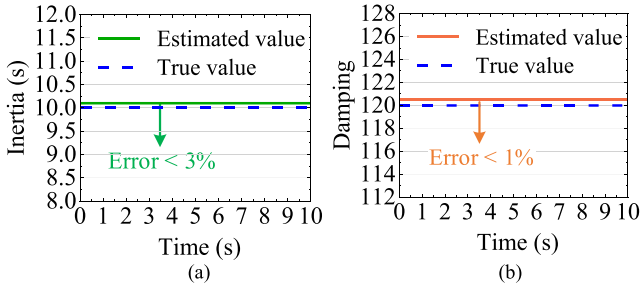

Fig. 8. Simulation results of the inertia and damping estimation with matching control, including the (a) inertia coefficient of 10 s and (b) damping coefficient of 120.

indicate that the estimation errors remain within 3% . These errors originate from slight deviations in the frequency and RoCoF measurements, which were introduced during the frequency estimation process due to the inclusion of virtual impedances. In experiments, to avoid this problem, we deliberately selected a large grid-side inductance of the testing equipment, with parameters listed in Table II. A more detailed description of the testing process will be provided later.

Furthermore, the proposed method is applied to the GFMCs with other control strategies to validate its universality. The simulation results of the equivalent damping estimation with droop control are presented in Fig. 7, while the simulation results of the inertia and damping estimation with matching control are shown in Fig. 8. As illustrated in the Figs. 7 and 8, the damping estimation errors are less than 1% , and the inertia estimation error is below 3% . Notably, since droop control does not provide an inertia coefficient, the relevant inertia estimation is not discussed. Nevertheless, the proposed method can still estimate an equivalent damping coefficient, which is the inverse of the droop coefficient.

In addition, as analyzed in Section III, the coupling of damping and inertial power affects the accuracy of inertia estimation. For verification, we conducted comparative analysis through the simulations of six cases with different inertia coefficients (from 6 s to 10 s with a step of 1 s), where the RoCoF changes with 0.01 Hz/s, and the damping coefficient is 1. As shown in Figs. 9 and 10, without power decoupling, the estimation results are highly inaccurate with noticeable errors, making inertia coefficient estimation impossible. Alternatively, the proposed power decoupling method limits the estimation error within 3%. Therefore, power decoupling is essential and must be considered.

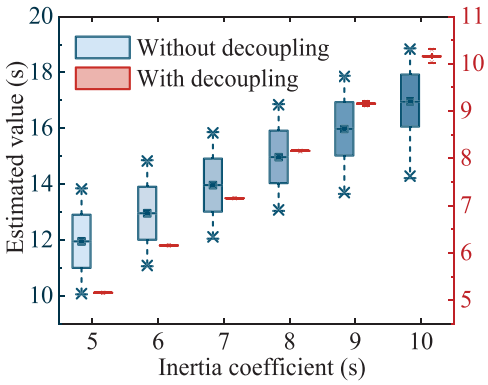

Fig. 9. Comparisons of simulation results for inertia coefficient estimation with and without power decoupling.

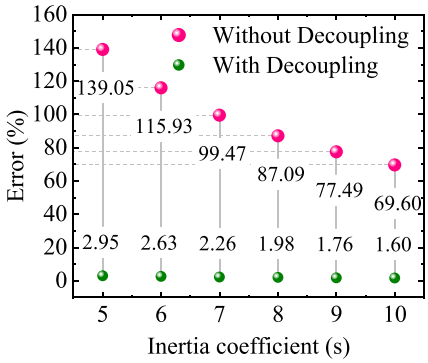

Fig. 10. Comparisons of estimation errors for inertia coefficient estimation with and without power decoupling.

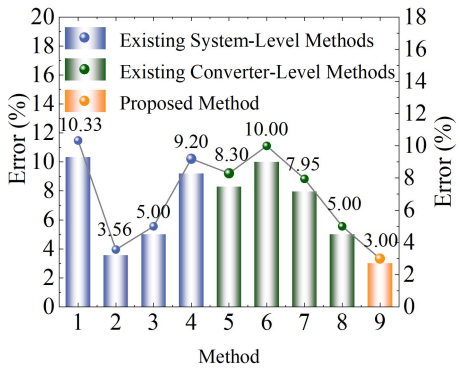

Fig. 11. Comparisons of measurement accuracy between the proposed method and existing methods.

To further highlight the advantage of the proposed method, the comparisons between the proposed method and existing methods are presented in Fig. 11, including both system-level and converter-level methods. Specifically, Methods 1–4 are system-level methods, where Method 1 uses natural disturbances, Method 2 adds active disturbances, Method 3 employs data-driven techniques, and Method 4 relies on analytical modeling. Methods 5–8 correspond to converter-level methods, in which Methods 5 and 6 are model-based, while Methods 7 and 8 adopt data-driven strategies. Method 9 represents the proposed method. The comparison results indicate that the proposed method benefits from the smallest errors.

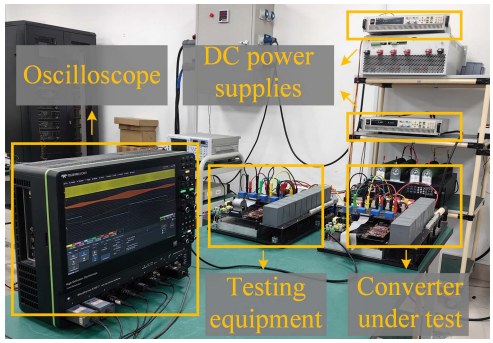

Fig. 12. Photograph of the experimental setup.

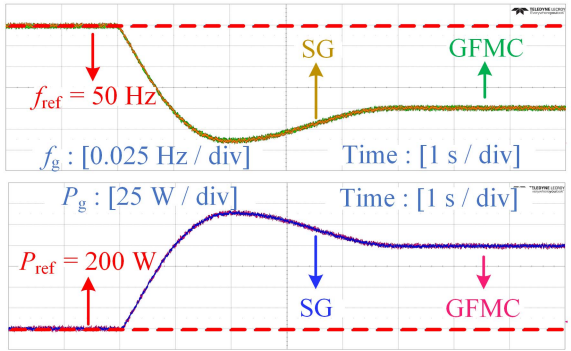

Fig. 13. Comparison of (a) frequency and (b) active power waveforms of an SG and a GFMC with $H_g = 5$ s and $D_g = 50$.

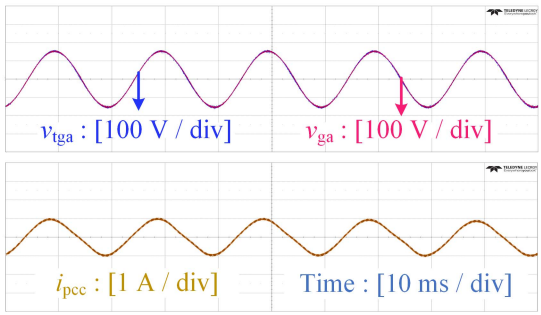

Fig. 14. Voltage and current experimental waveforms of the GFMC under test and the testing equipment.

B. Experimental Results

To further verify the proposed method, experiments were carried out based on the system schematic diagram shown in Fig. 1 and parameters listed in Table II. Fig. 12 shows a photo of the experimental setup, which includes two GFMCs, their power supplies, and an oscilloscope. To verify that the setup can emulate the inertia and damping of an SG, the comparisons of the power–frequency experimental waveforms of an SG and a GFMC are shown in Fig. 13. Next, Fig. 14 shows the voltage and current waveforms after the parallel connection of two GFMCs, where only Phase A components are given for simplicity. Before testing, the voltage magnitudes and phase angles of two converters almost overlap.

First, experimental tests were conducted for the converter with the VSM control. For testing the damping coefficient, we

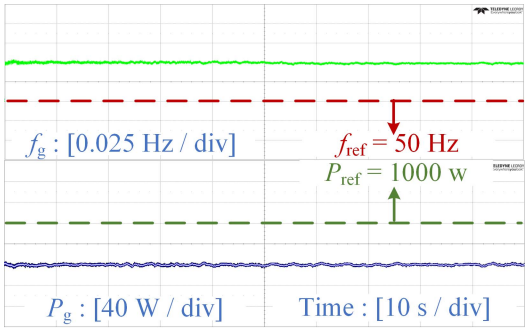

Fig. 15. Frequency and power experimental waveforms during the damping test.

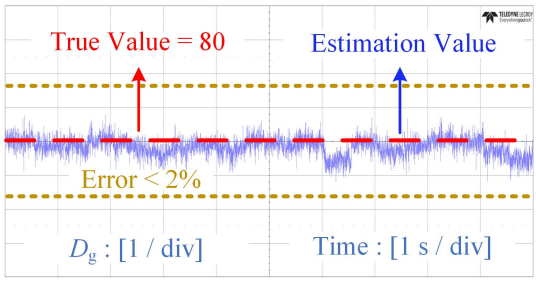

Fig. 16. Damping experimental estimation result for a damping coefficient of 80.

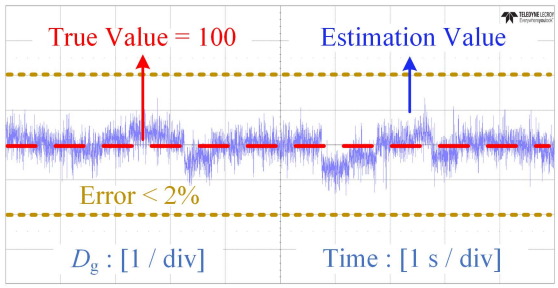

Fig. 17. Damping experimental estimation result for a damping coefficient of 100.

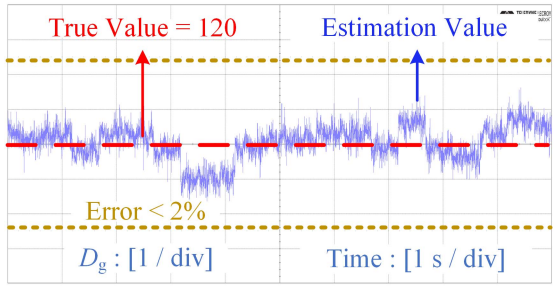

Fig. 18. Damping experimental estimation result for a damping coefficient of 120.

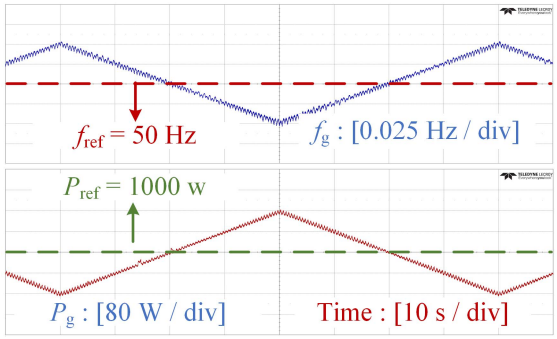

Fig. 19. Frequency and active power (including inertial power and damping power) experimental waveforms during the inertia test.

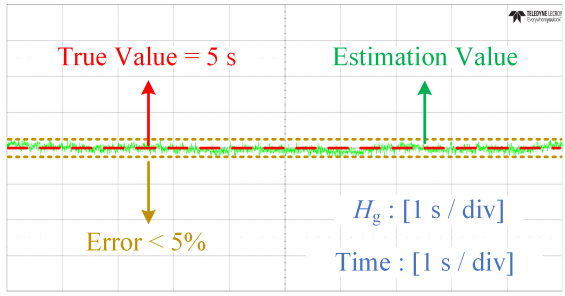

Fig. 20. Inertia experimental estimation result for an inertia coefficient of 5 s.

changed the frequency of the testing equipment from 50 Hz to 50.05 Hz. After that, the measurement blocks of the testing equipment obtained the frequency and power signals. Fig. 15 shows the frequency and power changes of the GFMC under test, which vary in reverse proportion. According to (5), the damping coefficient can then be calculated. We conducted tests for three different damping coefficients of 80, 100, and 120. Figs. 16 –18 present the experimental results, where all errors remain within 2% .

For testing the inertia coefficient, the testing equipment's frequency varies uniformly within the range of 50±0.1 Hz, following a bipolar triangular waveform with a period of 80 s. This provides linear frequency variations and a constant RoCoF, thereby simplifying RoCoF computation, suppressing measurement noise, and maximizing frequency excursions to minimize relative errors while ensuring system stability. During this process, the active power, which includes both inertial power and damping power, exhibits variations opposite to those of the frequency, as shown in Fig. 19. According to (3), these two power components can be decoupled, thus allowing the inertia coefficient to be calculated. Notably, this step is crucial for accurate inertia coefficient estimation, as the coupling between inertia and damping often leads to significant errors in inertia coefficient measurement.

Three tests were conducted for inertia coefficients of 5 s, 8 s, and 10 s, with all testing errors within 5% , as illustrated in Figs. 20 –22. These experiments provide strong evidence for the effectiveness of the proposed method.

Next, the proposed method is applied to other control strategies. The equivalent damping estimation experimental results with droop control are presented in Figs. 23 and 24, while the inertia and damping estimation experimental results with matching control are shown in Figs. 25 and 26. In both cases, the damping estimation errors are less than 2% . For matching control, the inertia estimation error is below 5% .

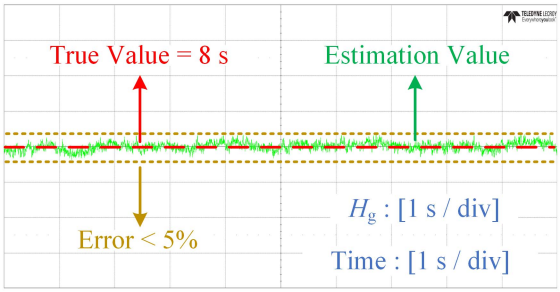

Fig. 21. Inertia experimental estimation result for an inertia coefficient of 8 s.

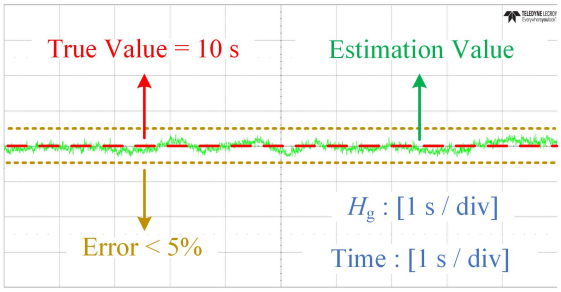

Fig. 22. Inertia experimental estimation result for an inertia coefficient of 10 s.

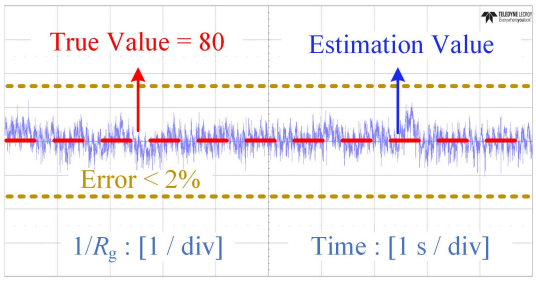

Fig. 23. Experimental result for a droop coefficient R_g of 0.0125.

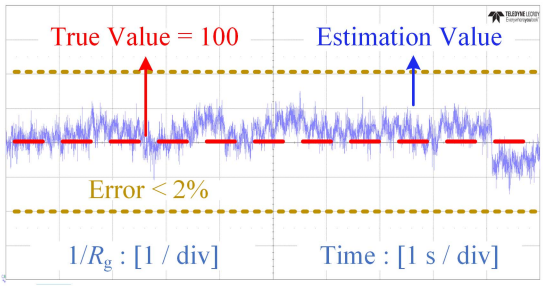

Fig. 24. Experimental result for a droop coefficient R_g of 0.01.

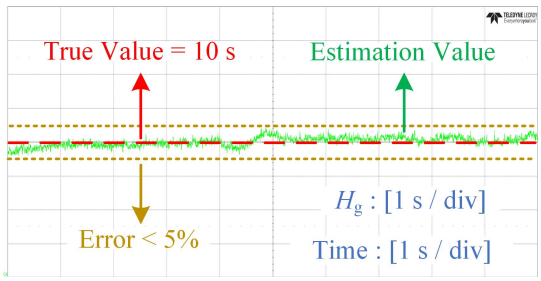

Fig. 25. Inertia experimental estimation result for matching control with an inertia coefficient of 10 s.

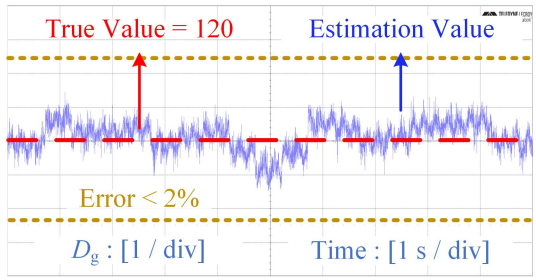

Fig. 26. Damping experimental estimation result for matching control with a damping coefficient of 120.

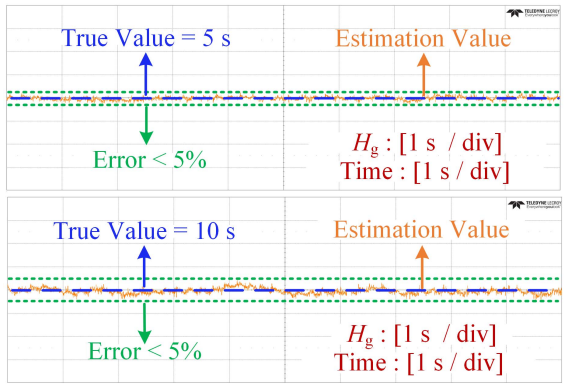

Fig. 27. Real-time experimental estimation results for inertia coefficients of 5 s and 10 s.

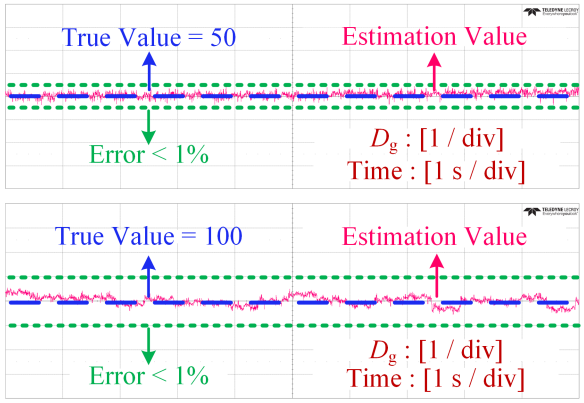

Fig. 28. Real-time experimental estimation results for damping coefficients of 50 and 100.

Furthermore, since the proposed method relies on the power–frequency relationship, the accurate real-time estimation of the inertia and damping coefficients is possible. The relevant experimental results are shown in Figs. 27 and 28, where the damping estimation errors remain below 1% and the inertia estimation errors are within 5% .

VI. Experimental Data Processing

Noise and disturbances in experiments can degrade frequency measurement and inertia estimation accuracy. To improve accuracy, we design data-processing procedures, including filtering, averaging, and optimal time-window selection, which ensure

that the estimation of inertia and damping coefficients relies on stable information. Since inertia estimation involves RoCoF and is sensitive to frequency errors, the subsequent data-processing discussion focuses on inertia estimation.

First, the frequency and power measurement signals are filtered to remove high-frequency noise. In this article, we employ a second-order low-pass Butterworth filter, which is designed to achieve a maximally flat amplitude response within the passband [40]. The magnitude response of an n-th order Butterworth filter can be expressed as follows [41]:

$$|H(j\omega)| = \frac{1}{\sqrt{1+(\omega/\omega_c)^{2n}}} \tag{7}$$

where ω_c represents the cutoff frequency of the filter, and n is the filter order.

For simplicity, we consider the standard second-order form, which is expressed as follows.

$$H(s) = \frac{1}{s^2+\sqrt{2}\omega_c s+\omega_c^2}. \tag{8}$$

The resulting filtered power and frequency signals are given as follows.

$$\tilde{P}_{\mathrm{g}}(t) = \mathcal{L}^{-1}\left\{H(s)\cdot\mathcal{L}\left\{P_{\mathrm{g}}(t)\right\}\right\} \tag{9}$$

$$\tilde{f}_{\mathrm{g}}(t) = \mathcal{L}^{-1}\left\{H(s)\cdot\mathcal{L}\left\{f_{\mathrm{g}}(t)\right\}\right\} \tag{10}$$

where $P_{\mathrm{g}}(t)$ and $f_{\mathrm{g}}(t)$ denote the measured power and frequency signals before filtering, and $\tilde{P}_{\mathrm{g}}(t)$ and $\tilde{f}_{\mathrm{g}}(t)$ represent the corresponding signals after filtering.

Second, to mitigate the influence of measurement noise on frequency derivative, a moving-average scheme is applied. Specifically, the RoCoF is calculated as the difference between the average frequencies at the beginning and end of a 0.5-s observation window via

$$f_{\mathrm{RoCoF}}(t) = \frac{\bar{f}_{\mathrm{end}}\left(t+\frac{1}{2}T_{\mathrm{w}}\right)-\bar{f}_{\mathrm{start}}\left(t-\frac{1}{2}T_{\mathrm{w}}\right)}{T_{\mathrm{w}}} \tag{11}$$

where T_{w} is the window length, f_{end} and f_{start} denote the average frequency over the last and first N samples within the window, respectively,

$$\bar{f}_{\mathrm{end}}\left(t+\frac{1}{2}T_{\mathrm{w}}\right) = \frac{1}{N}\sum_{i=0}^{N-1}\tilde{f}_{\mathrm{g}}\left(t+\frac{1}{2}T_{\mathrm{w}}-i\cdot\Delta t\right) \tag{12}$$

$$\bar{f}_{\mathrm{start}}\left(t-\frac{1}{2}T_{w}\right) = \frac{1}{N}\sum_{i=0}^{N-1}\tilde{f}_{g}\left(t-\frac{1}{2}T_{w}+i\cdot\Delta t\right). \tag{13}$$

In (12) and (13), Δt refers to the sampling interval. Given the slow and nearly linear frequency variation, this approach yields smoothed and noise-robust RoCoF estimation by mitigating instantaneous measurement noise.

Third, a 0.5-s observation window is used to compute the average changes in power and frequency within the window, as shown below.

$$\bar{f}_{\mathrm{g}}(t) = \frac{1}{M}\sum_{i=0}^{M-1}\tilde{f}_{\mathrm{g}}(t-i\cdot\Delta t) \tag{14}$$

$$\bar{P}_{\mathrm{g}}(t) = \frac{1}{M}\sum_{i=0}^{M-1}\tilde{P}_{\mathrm{g}}(t-i\cdot\Delta t) \tag{15}$$

where M represents the number of sampling points corresponding to the 0.5 s window.

Finally, the active power and frequency data processed in the previous steps are substituted into the inertia coefficient estimation equation in (6).

Notably, the proposed testing method is primarily designed as a converter-level approach for the offline testing of GFMCs. At the converter level, the key objective is to accurately evaluate a converter's grid-forming capability, which improves grid integration security, ancillary service provision, and standardization. Under this context, the accuracy outweighs speed, and a 0.5-s window provides sufficient resolution to meet the practical needs of manufacturers, operators, and regulators.

VII. Conclusion

This article proposes a novel, simple, and effective model-based method for measuring the inertia and damping coefficients of GFMCs, which explicitly considers the coupling between inertial and damping power, thereby improving estimation accuracy. In parallel, this article develops the first testing equipment specifically designed for GFMCs. Furthermore, the accuracy of the proposed method is experimentally validated through a setup consisting of the developed testing equipment and a GFMC under test, which record $\geq$95% inertia estimation accuracy and $\geq$98% damping estimation accuracy.

References

[1] M. Rehmani, M. Reisslein, A. Rachedi, M. Kantarci, and M. Radenkovic, "Integrating renewable energy resources into the smart grid: Recent developments in information and communication technologies," *IEEE Trans. Ind. Inf.*, vol. 14, no. 7, pp. 2814–2825, Jul. 2018.

[2] F. Milano, F. Dörfler, G. Hug, D. Hill, and G. Verbič, "Foundations and challenges of low-inertia systems (invited paper)," in *Proc. Power Syst. Comput. Conf.*, Dublin, Ireland, 2018, pp. 1–25.

[3] J. Fang, H. Li, Y. Tang, and F. Blaabjerg, "On the inertia of future more-electronics power systems," *IEEE J. Emerg. Sel. Top. Power Electron.*, vol. 7, no. 4, pp. 2130–2146, Dec. 2019.

[4] H. Zhang, W. Xiang, W. Lin, and J. Wen, "Grid forming converters in renewable energy sources dominated power grid: Control strategy, stability, application, and challenges," *J. Mod. Power Syst. Clean Energy*, vol. 9, no. 6, pp. 1239–1256, Nov. 2021.

[5] L. Fernandes, M. Paternina, D. Dotta, and J. Chow, "Data-driven assessment of center of inertia and regional inertia content considering load contribution," *Int. J. Electr. Power Energy Syst.*, vol. 156, pp. 0142–0615, Feb. 2024.

[6] B. Poolla, S. Bolognani, N. Li, and F. Dörfler, "A market mechanism for virtual inertia," *IEEE Trans. Smart Grid*, vol. 11, no. 4, pp. 3570–3579, Jul. 2020.

[7] A. Dyśko et al., "Testing characteristics of grid forming converters part III: Inertial behaviour," in *Proc. 19th Wind Integration Workshop*, 2020, pp. 1–8.

[8] P. M. Ashton, C. S. Saunders, G. A. Taylor, A. M. Carter, and M. E. Bradley, "Inertia estimation of the GB power system using synchrophasor measurements," *IEEE Trans. Power Syst.*, vol. 30, no. 2, pp. 701–709, Mar. 2015.

[9] J. Schiffer, P. Aristidou, and R. Ortega, "Online estimation of power system inertia using dynamic regressor extension and mixing," *IEEE Trans. Power Syst.*, vol. 34, no. 6, pp. 4993–5001, Nov. 2019.

[10] Y. Susuki, R. Hamasaki, and A. Ishigame, "Estimation of power system inertia using nonlinear Koopman modes," in *Proc. IEEE Power Energy Soc. Gen. Meet.*, Portland, USA, 2018, pp. 1–5.

[11] D. Yang et al., "Data-driven estimation of inertia for multiarea interconnected power systems using dynamic mode decomposition," *IEEE Trans. Ind. Inf.*, vol. 17, no. 4, pp. 2686–2695, Apr. 2021.
[12] N. Hosaka, B. Berry, and S. Miyazaki, "The world's first small power modulation injection approach for inertia estimation and demonstration in the island grid," in *Proc. Int. Conf. Renewable Energy Res. Appl.*, Brasov, Romania, 2019, pp. 722–726.
[13] J. Zhang and H. Xu, "Online identification of power system equivalent inertia constant," *IEEE Trans. Ind. Electron.*, vol. 64, no. 10, pp. 8098–8107, Oct. 2017.
[14] R. J. Best, P. V. Brogan, and D. J. Morrow, "Power system inertia estimation using HVDC power perturbations," *IEEE Trans. Power Syst.*, vol. 36, no. 3, pp. 1890–1899, May 2021.
[15] A. Poudyal, U. Tamrakar, R. D. Trevizan, R. Fourney, R. Tonkoski, and T. M. Hansen, "Multiarea inertia estimation using convolutional neural networks and federated learning," *IEEE Syst. J.*, vol. 16, no. 4, pp. 6401–6412, Dec. 2022.
[16] J. Guo, X. Wang, and B. Ooi, "Online purely data-driven estimation of inertia and center-of-inertia frequency for power systems with VSC-interfaced energy sources," *Int. J. Electr. Power Energy Syst.*, vol. 137, pp. 0142–0615, May 2022.
[17] A. Schmitt and B. Lee, "Steady-state inertia estimation using a neural network approach with modal information," in *Proc. IEEE Power Energy Soc. Gen. Meet.*, Chicago, USA, 2017, pp. 1–5.
[18] A. Gorbunov, A. Dymarsky, and J. Bialek, "Estimation of parameters of a dynamic generator model from modal PMU measurements," *IEEE Trans. Power Syst.*, vol. 35, no. 1, pp. 53–62, Jan. 2020.
[19] K. Tuttelberg, J. Kilter, D. Wilson, and K. Uhlen, "Estimation of power system inertia from ambient wide area measurements," in *Proc. IEEE Power Energy Soc. Gen. Meet.*, Atlanta, USA, 2019, pp. 1–1.
[20] B. Wang et al., "Power system inertia estimation method based on maximum frequency deviation," *IET Renew. Power Gener.*, vol. 16, no. 3, pp. 622–633, Feb. 2022.
[21] M. Xie, J. She, Z. T. Liu, and D. Y. Li, "Online estimation of moment of inertia incorporating disturbance estimation," *IEEE Trans. Ind. Electron.*, vol. 71, no. 7, pp. 7610–7620, Jul. 2024.
[22] C. Lian, F. Xiao, S. Gao, and J. Liu, "Load torque and moment of inertia identification for permanent magnet synchronous motor drives based on sliding mode observer," *IEEE Trans. Power Electron.*, vol. 34, no. 6, pp. 5675–5683, Jun. 2019.
[23] H. Deng, J. Fang, Y. Qi, Y. Tang, and V. Debusschere, "A generic voltage control for grid-forming converters with improved power loop dynamics," *IEEE Trans. Ind. Electron.*, vol. 70, no. 4, pp. 3933–3943, Apr. 2023.
[24] S. Dimoulias, E. Kontis, and G. Papagiannis, "Inertia estimation of synchronous devices: Review of available techniques and comparative assessment of conventional measurement-based approaches," *Energies*, vol. 15, no. 20, Sep. 2022, Art. no. 7767.
[25] P. Hu, Y. Li, and Y. Yu, "Inertia estimation of renewable-energy-dominated power system," *Renewable Sustain. Energy Rev.*, vol. 183, Sep. 2023, Art. no. 113481.
[26] X. Liu and Y. Li, "Inertia identification for grid-forming converter based on model-data hybrid-driven method," in *Proc. IEEE Int. Conf. Energy Internet*, Zhuhai, China, 2024, pp. 743–747.
[27] J. Guo, X. Wang, and B. T. Ooi, "Estimation of inertia for synchronous and non-synchronous generators based on ambient measurements," *IEEE Trans. Power Syst.*, vol. 37, no. 5, pp. 3747–3757, Sep. 2022.
[28] M. Liu, J. Chen, and F. Milano, "On-line inertia estimation for synchronous and non-synchronous devices," *IEEE Trans. Power Syst.*, vol. 36, no. 3, pp. 2693–2701, May 2021.
[29] Y. Li, P. Hu, Y. Cao, and Y. Yu, "Virtual inertia estimation for grid-forming converter based on deep reinforcement learning method," in *Proc. IEEE Int. Electr. Energy Conf.*, Harbin, China, 2024, pp. 1946–1951.
[30] B. Tan and J. Zhao, "Data-driven time-varying inertia estimation of inverter-based resources," *IEEE Trans. Power Syst.*, vol. 38, no. 2, pp. 1795–1798, Mar. 2023.
[31] H. Alvand, A. Zare, M. Shadmand, and S. Mazumder, "AI-based effective virtual inertia estimation in a meshed network of inverters," in *Proc. IEEE Ind. Electron. Soc. Annu. Conf.*, Chicago, IL, USA, 2024, pp. 1–6.
[32] J. Li, L. Yang, Z. Xu, W. Liu, Q. Zhu, and F. Xu, "Inertia estimation method for VSG-dominated power system based on improved extended kalman filter," in *Proc. IEEE Power Electron. Syst. Appl.*, Hongkong, 2024, pp. 1–6.
[33] Q. Ma, C. Liu, and J. Fang, "Grid-forming cascaded-bridge converters with parallel connectivity," *IEEE Trans. Ind. Electron.*, vol. 72, no. 12, pp. 13475–13486, Dec. 2025, doi: 10.1109/TIE.2025.3587124.
[34] H. Beck and R. Hesse, "Virtual synchronous machine," in *Proc. 9th Int. Conf. Elect. Power Qual. Utilisation*, Barcelona, Spain, Oct. 2007, pp. 1–6.
[35] S. Arco and J. A. Suul, "Equivalence of virtual synchronous machines and frequency-droops for converter-based microgrids," *IEEE Trans. Smart Grid*, vol. 5, no. 1, pp. 394–395, Jan. 2014.
[36] S. Arco and J. Suul, "Virtual synchronous machines—Classification of implementations and analysis of equivalence to droop controllers for microgrids," in *Proc. IEEE Grenoble Conf.*, Grenoble, France, 2013, pp. 1–7.
[37] J. Liu, Y. Miura, and T. Ise, "Comparison of dynamic characteristics between virtual synchronous generator and droop control in inverter-based distributed generators," *IEEE Trans. Power Electron.*, vol. 31, no. 5, pp. 3600–3611, May 2016.
[38] J. A. Suul, S. Arco, and G. Guidi, "Virtual synchronous machine-based control of a single-phase bi-directional battery charger for providing vehicle-to-grid services," *IEEE Trans. Ind. Appl.*, vol. 52, no. 4, pp. 3234–3244, Jul./Aug. 2016.
[39] H. Bevrani, T. Ise, and Y. Miura, "Virtual synchronous generators: A survey and new perspectives," *Int. J. Electr. Power Energy Syst.*, vol. 54, pp. 244–254, Jan. 2014.
[40] S. Butterworth, "On the theory of filter amplifiers," *Wireless Eng.*, vol. 7, no. 6, pp. 536–541, Mar. 1930.
[41] A. Acharya, S. Das, and I. Pan, "Extending the concept of analog Butterworth filter for fractional order systems," *Signal Process.*, vol. 94, pp. 409–420, Jan. 2014.

Yufan Wang (Student Member, IEEE) received the B.Eng. degree in automation from Shandong University, Jinan, China, in 2021, where she is currently working toward the Ph.D. degree in electronic information

Her research interests focus on grid-forming capability estimation, with a focus on measurement methodologies and control strategies.

Jingyang Fang (Senior Member, IEEE) received the B.Sc. and M.Sc. degrees in electrical engineering from Xi'an Jiaotong University, Xi'an, China, in 2013 and 2015, respectively, and the Ph.D. degree in electrical engineering from the School of Electrical and Electronic Engineering, Nanyang Technological University, Singapore, in 2019.

From May to August 2018, he was a Visiting Scholar with the Institute of Energy Technology, Aalborg University, Aalborg, Denmark. From 2018 to 2019, he was a Research Fellow with the School of Electrical and Electronic Engineering, Nanyang Technological University. From 2019 to 2021, he was a Postdoctoral Researcher with the Duke University and TU Kaiserslautern. Since 2021, he has been working as a Full Professor with the School of Control Science and Engineering, Shandong University. His research interests include power quality control, stability analysis and improvement, renewable energy integration, and digital control in more-electronics power systems. Dr. Fang was the recipient of the Humboldt Research Fellowship, National Excellent Young Scientists (Overseas), two IEEE Prize Paper Awards, one Best Presenter Award, the IEEE JESTPE Star Reviewer Award, the Chinese Government Award for Outstanding Self-Financed Students Abroad in 2018, and the Best Thesis Award from NTU in 2019. He was World's Top 2% Highly Cited Scientists ranked by Stanford University.